


## White-noise-induced double coherence resonances in reduced Hodgkin-Huxley neuron model near subcritical Hopf bifurcation

Li Li 

Guangdong Key Laboratory of Modern Control Technology, Institute of Intelligent Manufacturing,  
Guangdong Academy of Sciences, Guangzhou 510070, China

Zhiguo Zhao \*

School of Science, Henan Institute of Technology, Xinxiang 453003, China

 (Received 21 November 2021; revised 22 February 2022; accepted 4 March 2022; published 21 March 2022)

Coherence resonance (CR) describes a counterintuitive phenomenon in which the optimal oscillatory responses in nonlinear systems are shaped by a suitable noise amplitude. This phenomenon has been observed in neural systems. In this research, the generation of double coherence resonances (DCRs) due to white noise is investigated in a three-dimensional reduced Hodgkin-Huxley neuron model with multiple-timescale feature. We show that additive white noise can induce DCRs from the resting state near a subcritical Hopf bifurcation. The appearance of DCRs is related to the changes of the firing pattern aroused by the increases of the noise amplitude. The underlying dynamical mechanisms for the appearance of the DCRs and the changes of the firing pattern are interpreted using the phase space analysis and the dynamics of the stable focus-node near the subcritical Hopf bifurcation. We find that the multiple-timescale dynamics is essential for generating the DCRs and different firing patterns. The results not only present a case in which noise can induce DCRs near a Hopf bifurcation but also provide its dynamical mechanism, which enriches the phenomena in nonlinear dynamics and provides further understanding on the roles of noise in neural systems with multiple-timescale feature.

DOI: [10.1103/PhysRevE.105.034408](https://doi.org/10.1103/PhysRevE.105.034408)

### I. INTRODUCTION

Noise is ubiquitous in real-world systems and usually produces undesirable disturbances or fluctuations [1]. In contrast to the undesirable effects, it has been demonstrated that noise can play constructive roles in nonlinear systems, where stochastic resonance or coherence resonance (CR) is the classic phenomenon [2–5]. Suitable noise intensity can enhance the sensitivity of a system to weak external stimulation [5], and optimal noise intensity can induce a coherent oscillatory response [3,4]. Stochastic resonance and CR have been found in distinct systems such as the laser systems [6], quantum systems [7], chemical systems [8], and thermoacoustic systems [9], especially in the neuronal systems. In the neuronal systems, both phenomena have been identified in various neurons, including cat visual neurons, cricket cercal sensory neurons, and human muscle spindles [10,11]. Due to the positive roles of noise, stochastic resonance or CR [12] has been applied in the field of biomedical applications such as the enhancement of lower-limb cutaneous reflex responses and vestibulospinal reflexes, the improvement of sensorimotor control, and perceptual decision-making [13–15]. This shows that it is essential to study stochastic resonance or CR for understanding their roles and the underlying mechanisms.

CR has been extensively studied in the neuronal systems, including neuronal networks not just single neurons.

Researchers have focused on the intrinsic characteristics of single neurons and the features of neuronal networks to better understand the generation mechanisms. In single neurons, the generation mechanisms of the CR aroused by various noises in neuronal models with different bifurcation points have been studied, such as the white noise in spiking neuron models including the classic Hodgkin-Huxley (HH) [16,17], Morris-Lecar [18], and Fitzhugh-Nagumo [4,19–22] neuron models and white noise, Ornstein-Uhlenbeck noise, and quasimonochromatic noise in bursting neuron models [23–26] such as the Hindmarsh-Rose neuron model [27]. Different bifurcations in these neuron models signify the different generation mechanisms of the CR. In neuronal networks, the coupling strength, network structure, synaptic types, and time delay are used to investigate the influence on CR [7,28–34]. For instance, the CR can be enhanced as the coupling strength or time delay increases [35,36]. The degree of coherence response can be enhanced by adding shortcut links in a small-world network [37].

In most research results, only one CR in neuronal systems is aroused as noise intensity increases. For example, a single CR is induced by white noise from the resting state near the Hopf bifurcation [4,6,16,20,38] or the saddle node bifurcation of the limit cycles [16,18,39–41] or near the bursting state [26]. In contrast to single CR, DCRs can be induced by noise when neuron models with different dynamical characteristics or other types of noise are considered. For example, phase noise can induce DCRs in single neuron models near the Hopf bifurcation [42–44]. DCRs in the Rulkov discrete

\*zzg164637758@163.com

model are evoked from subthreshold oscillations by additive or multiplicative noises [45]. Doubly stochastic coherence is observable in Fitzhugh–Nagumo neuron model with both additive noise and multiplicative noise [46,48]. DCRs are also observable when inhibitory or excitatory correlated stimuli is considered [49]. In addition, other factors of neuronal systems such as synaptic characteristics and the properties of the network can evoke CR or multiple CRs [50]. For example, multiple CRs appear in neuronal networks with the increase of the time delay in synapses or autapses [17,21,35,51–53]. In addition to a noise-induced CR, with the help of noise, CR can also be induced by increasing the connection probability of nearby layers in feedforward networks [54].

In this research, the effect of white noise on CR in a reduced HH neuron model is studied near a subcritical Hopf bifurcation. We find that DCRs are aroused from the resting state near the subcritical Hopf bifurcation as the noise amplitude increases, which is different from the previous results that white noise induces a CR near a Hopf bifurcation in single neuron models [4,6,16,20,38] and the appearance of DCRs requires multiple external stimuli such as simultaneous presence of additive noise and multiplicative noise [46–49]. These results not only enrich the phenomena of nonlinear dynamics but also present a different understanding about the roles of noise in neural systems. In addition, we find that the changes of the firing patterns have a relationship with the transition of the DCRs. Based on the multiple-timescale dynamics of the reduced HH neuron model and the dynamics of stable focus-node near the Hopf bifurcation, the underlying dynamical mechanisms for the changes of firing patterns induced by noise are investigated to interpret the DCR phenomena. Specifically, with the fluctuation of weak noise, the trajectory near the stable focus-node rotates multiple times to form small amplitude oscillations, and the trajectory crosses over the threshold surface near the focus-node to form a spike, i.e., mixed-mode oscillations (MMOs) that consist of alternation between a spike and multiple small amplitude oscillations are induced, hereafter referred to as class 1 MMOs. With the increase of the noise amplitude, the firing pattern of the class 1 MMOs becomes more regular due to the decrease of interspike intervals (ISIs). For a larger noise amplitude, some trajectories can cross over the threshold surface far away from the stable focus-node to form a cluster of spikes. MMOs that are random alternation of a spike, a cluster of spikes, and multiple small amplitude oscillations, are generated. These MMOs are called class 2 MMOs in this paper. In other words, class 2 MMOs are composed of successive spiking and class 1 MMOs. The random appearance of successive spiking destroys the coherence of the firing pattern of the class 1 MMOs. With the further increase of the noise amplitude, the firing pattern is mainly composed of successive spiking and returns as a regular mode. For stronger noise, great fluctuations of the trajectories aroused by the noise result in the decrease of coherence. Similar results are also observed in the classic HH neuron models with multiple-timescale feature.

The present paper is organized as follows. Deterministic and stochastic reduced HH models, the methods used in the paper, and the measurements used to characterize CR are presented in Sec. II. The results of the effect of white noise

on the CR of the reduced HH neuron model are presented in Sec. III. Discussions and conclusions are presented in Sec. IV.

## II. MODELS, METHODS, AND MEASUREMENTS

### A. Deterministic models

The classic HH neuron model first accurately describes the generation and propagation of action potentials in the giant axon of a squid and is generally used to study cellular functions such as neural encoding. The classic HH model contains four variables: membrane potential  $V$ , activation variable  $m$  and inactivation variable  $h$  of a sodium current, and activation variable  $n$  of a potassium current. The variables  $V$  and  $m$  evolve on a fast timescale, and the variables  $h$  and  $n$  evolve on a slow timescale. The classic HH neuron model is as follows:

$$C \frac{dV}{dt} = -g_{\text{Na}} m^3 h (V - E_{\text{Na}}) - g_{\text{K}} n^4 (V - E_{\text{K}}) - g_{\text{L}} (V - E_{\text{L}}) + I_{\text{app}}, \quad (1)$$

$$\frac{dm}{dt} = \frac{\alpha_m (1 - m) - \beta_m}{\tau_m}, \quad (2)$$

$$\frac{dh}{dt} = \frac{\alpha_h (1 - h) - \beta_h}{\tau_h}, \quad (3)$$

$$\frac{dn}{dt} = \frac{\alpha_n (1 - n) - \beta_n}{\tau_n}, \quad (4)$$

with

$$\alpha_m(V) = 0.1(V + 40)/\{1 - \exp[-0.1(V + 40)]\},$$

$$\beta_m(V) = 4 \exp[-(V + 65)/18],$$

$$\alpha_h(V) = 0.07 \exp[-(V + 65)/20],$$

$$\beta_h(V) = 1/\{1 + \exp[-0.1(V + 35)]\},$$

$$\alpha_n(V) = 0.01(V + 55)/\{1 - \exp[-0.1(V + 55)]\},$$

$$\beta_n(V) = 0.125 \exp[-(V + 65)/80].$$

To make analysis easier, some neuron models modified from the classic HH neuron model are proposed [56]. A three-dimensional (3D) reduced model [55] with the steady-state function  $m_{\infty}(V) = \alpha_m(V)/[\alpha_m(V) + \beta_m(V)]$  replacing the fast activation variable  $m$  in the classic HH model, is proposed, as follows:

$$C \frac{dV}{dt} = -g_{\text{Na}} m_{\infty}^3 h (V - E_{\text{Na}}) - g_{\text{K}} n^4 (V - E_{\text{K}}) - g_{\text{L}} (V - E_{\text{L}}) + I_{\text{app}}, \quad (5)$$

$$\frac{dh}{dt} = \frac{\alpha_h (1 - h) - \beta_h}{\tau_h}, \quad (6)$$

$$\frac{dn}{dt} = \frac{\alpha_n (1 - n) - \beta_n}{\tau_n}. \quad (7)$$

The parameter values for the 3D HH model are taken from Ref. [55], and they are as follows: membrane capacitance  $C = 1.2 \mu\text{F}/\text{cm}^2$ , maximum conductance of the sodium current  $g_{\text{Na}} = 120 \text{ mS}/\text{cm}^2$ , maximum conductance of the potassium current  $g_{\text{K}} = 36 \text{ mS}/\text{cm}^2$ , maximum conductance of the leak current  $g_{\text{L}} = 0.3 \text{ mS}/\text{cm}^2$ , reversal potential of the sodium current  $E_{\text{Na}} = 50 \text{ mV}$ , reversal potential of the potassium current  $E_{\text{K}} = -77 \text{ mV}$ , reversal potential of the leak

current  $E_L = -54.4$  mV, and time constants  $\tau_h = 6$  and  $\tau_n = 1$ .  $I_{app}$  is the applied current. Unless otherwise stated,  $I_{app} = 8 \mu\text{A}/\text{cm}^2$  is selected as an example to present the results.

In addition to the replacement of the activation variable  $m$  by its steady-state function, the time constant  $\tau_h = 6$  used in this paper is different from the original HH neuron model. For the original HH neuron model, the time constant  $\tau_h$  is 1. When  $\tau_h$  is increased to 6, more complex dynamical behaviors such as MMOs are observed in the previous studies [55,56], which is because the time constant  $\tau_h = 6$  assures that the inactivation variable  $h$  evolves more slowly. The difference between the time constants  $\tau_h = 1$  and  $\tau_h = 6$  leads to that the dynamics of the 3D HH neuron model is different from the dynamics of the original HH neuron model. That is, the slower kinetic of  $h$  is responsible for the 3D HH neuron model to have dynamical properties different from the original HH neuron model. The 3D HH neuron model has a fast variable  $V$  and two slow variables  $h$  and  $n$ . In fact, the original HH neuron model can have the dynamics similar to the 3D HH neuron as  $\tau_h$  increases, which has been demonstrated in Ref. [56]. When  $\tau_m = 1$  and other parameter values for the classic HH neuron model (hereafter called four-dimensional (4D) HH neuron model) are the same as the 3D HH neuron model, the 4D HH model exhibits multiple-timescale feature and has dynamical behaviors that are similar to the 3D HH neuron model, as shown in the Appendix of the paper.

### B. Stochastic models

In this research, the Gaussian white noise  $\xi(t)$  is added to the right hand side of Eq. (5) to study the effect of the current noise on the firing process of the 3D HH model, and Eqs. (6) and (7) remain unchanged. Then, the 3D deterministic HH model becomes a 3D stochastic model, as follows:

$$C \frac{dV}{dt} = -g_{\text{Na}} m^3 h (V - E_{\text{Na}}) - g_{\text{K}} n^4 (V - E_{\text{K}}) - g_{\text{L}} (V - E_{\text{L}}) + I_{\text{app}} + D\xi(t), \quad (8)$$

where  $D$  is the noise amplitude. The Gaussian white noise  $\xi(t)$  satisfies  $\langle \xi(t) \rangle = 0$  and  $\langle \xi(t) \xi(t') \rangle = \delta(t - t')$ , where  $\langle \cdot \rangle$  symbolizes ensemble average, and  $\delta(\cdot)$  is the Dirac  $\delta$  function.

Similarly, the Gaussian white noise  $\xi(t)$  is added to the right hand side of Eq. (1) to study the effect of the current noise on the firing process of the 4D HH neuron model, and Eqs. (2)–(4) remain unchanged. Then, the 4D deterministic HH neuron model becomes a 4D stochastic model, where

$$C \frac{dV}{dt} = -g_{\text{Na}} m^3 h (V - E_{\text{Na}}) - g_{\text{K}} n^4 (V - E_{\text{K}}) - g_{\text{L}} (V - E_{\text{L}}) + I_{\text{app}} + D\xi(t). \quad (9)$$

In this paper, the 3D HH neuron model is mainly used to present the results. Similar results can also be obtained by using the 4D HH neuron model and are given in the Appendix.

### C. Methods

The bifurcation diagram [Fig. 1(a)] is obtained using XPPAUTO [57], the deterministic model is simulated by means of the Runge-Kutta method with a 0.01 ms step, and the

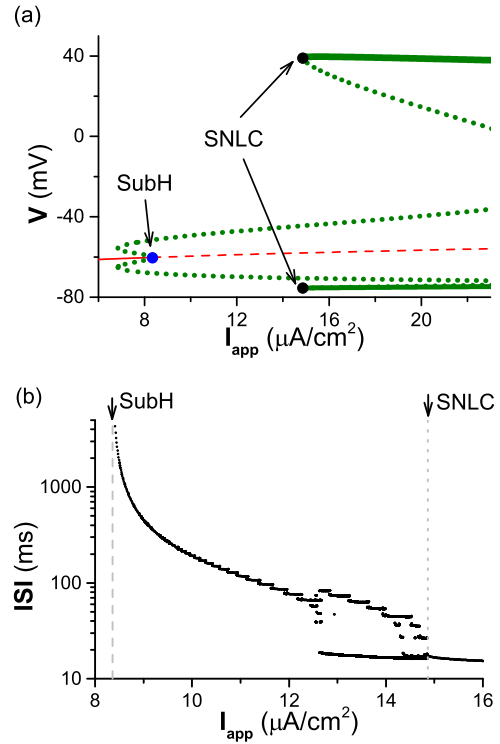


FIG. 1. Bifurcation diagram of the 3D deterministic HH model with the increase of  $I_{app}$ . (a) Bifurcations of equilibrium (red) and limit cycle (green). The red solid and dashed curves denote the stable and unstable equilibria, respectively. The green solid and dotted curves denote the maximum and minimum values of the stable and unstable limit cycles, respectively. The blue and black solid circles denote the bifurcation points of the subcritical Hopf bifurcation (SubH) and the saddle node bifurcation of the limit cycles (SNLC), respectively. (b) Other complex bifurcations of limit cycle when  $I_{app}$  is located between the bifurcation points SubH and SNLC

stochastic model is simulated by using the Euler-Maruyama method with a 0.001 ms step [58].

### D. Measurements of CR

The spike timing of neurons is of interest in neuroscience, because it is related to the temporal coding. Defining a sequence of spike times as  $t_i$ , the interspike interval (ISI) is  $T_i = t_{i+1} - t_i$ ,  $i = 1, 2, 3, \dots$ , where  $t_i$  and  $t_{i+1}$  are two contiguous spike times of spike trains. The coefficient of variation (CV) of the ISIs is a common measurement [59–61] used to characterize the spike train variability, and it is defined as

$$\text{CV} = \frac{\sqrt{\langle T_i^2 \rangle - \langle T_i \rangle^2}}{\langle T_i \rangle}.$$

The prominent minimum of CV at the optimal noise amplitude indicates the high degree of coherence of neuronal firing and is generally used to characterize CR. For the 3D stochastic HH model, 10 000 ISIs are simulated to plot the interspike interval histogram (ISIH) and to calculate the CV.

### III. RESULTS

#### A. Dynamical behaviors for the 3D deterministic HH neuron

For the 3D deterministic HH neuron model, the bifurcation diagram of the membrane potential with respect to  $I_{app}$  is as shown in Fig. 1(a). There is a unique equilibrium (red curve) even for a larger range of  $I_{app}$ . With the increase of  $I_{app}$ , the stable equilibrium (red solid curve) changes to an unstable equilibrium (red dashed curve) via a subcritical Hopf bifurcation (SubH, blue solid circle) at  $I_H := I_{app} \approx 8.359 \mu\text{A}/\text{cm}^2$ . A branch of unstable limit cycles (green dashed curve) is bifurcated from the Hopf bifurcation point SubH. The Hopf bifurcation-bifurcated unstable limit cycle collides with the stable limit cycle (green solid curve) at the point  $I_{app} \approx 14.86 \mu\text{A}/\text{cm}^2$  (black solid circles), which is a saddle-node bifurcation of the limit cycles (SNLC).

In addition to the above-mentioned bifurcations and dynamical behaviors, more complex bifurcations and dynamical behaviors are found in the interval between the bifurcation points SubH and SNLC, the detailed bifurcations can be found in Refs. [55,69]. The changes of the ISIs with respect to  $I_{app}$  are shown in Fig. 1(b). When  $8.359 \mu\text{A}/\text{cm}^2 < I_{app} < 14.18 \mu\text{A}/\text{cm}^2$ , the dynamical behavior for the 3D HH neuron model is single spike alternating with multiple small amplitude oscillations, i.e., MMOs. For example, when  $I_{app} = 9 \mu\text{A}/\text{cm}^2$  and  $I_{app} = 11.67 \mu\text{A}/\text{cm}^2$ , the firing patterns are as shown in Figs. 2(a) and 2(b), respectively. With the increase of  $I_{app}$ , the number of small amplitude oscillations within the ISIs decreases, which results in the decrease of the ISIs [Fig. 1(b)]. For example, when  $I_{app}$  increases from  $9 \mu\text{A}/\text{cm}^2$  to  $11.67 \mu\text{A}/\text{cm}^2$ , the ISIs are decreased from 459.34 ms to 76.38 ms. When  $14.18 \mu\text{A}/\text{cm}^2 < I_{app} < 14.86 \mu\text{A}/\text{cm}^2$ , the firing pattern of the 3D HH neuron is still MMOs. However, the MMOs are that a cluster of successive spikes alternate with multiple small amplitude oscillations. For example, when  $I_{app} = 14.2 \mu\text{A}/\text{cm}^2$ , the MMOs of two successive spikes alternating with several small amplitude oscillations are shown in Fig. 2(c). The ISI of the two successive spiking occurrences is around 16 ms, which is close to the period of the periodic repetitive spiking shown in Fig. 2(d) [corresponding to the stable limit cycle shown in Fig. 1(a)]. The ISIs for the MMOs, in which spikes are separated by small amplitude oscillations, are larger than 25 ms.

#### B. White-noise-induced DCRs

In this section, we describe the effect of white noise on the 3D HH neuron when it is excitable, i.e., when  $I_{app} < I_H \approx 8.359 \mu\text{A}/\text{cm}^2$ . Unless otherwise stated,  $I_{app} = 8 \mu\text{A}/\text{cm}^2$  is selected as representative to present the results.

##### 1. Noise induces different firing patterns

For the 3D HH neuron, noises with different amplitudes can induce different firing patterns from the resting state. The distinct firing patterns for six different noise amplitudes, including  $D = 0.1 \mu\text{A}/\text{cm}^2$ ,  $D = 0.4 \mu\text{A}/\text{cm}^2$ ,  $D = 0.6 \mu\text{A}/\text{cm}^2$ ,  $D = 1.3 \mu\text{A}/\text{cm}^2$ ,  $D = 7 \mu\text{A}/\text{cm}^2$ , and  $D = 20 \mu\text{A}/\text{cm}^2$ , are shown in Figs. 3(a)–3(f). When  $D = 0.1 \mu\text{A}/\text{cm}^2$ , the firing pattern of the 3D HH neuron is class 1 MMOs, that is, single spike alternates with multiple small

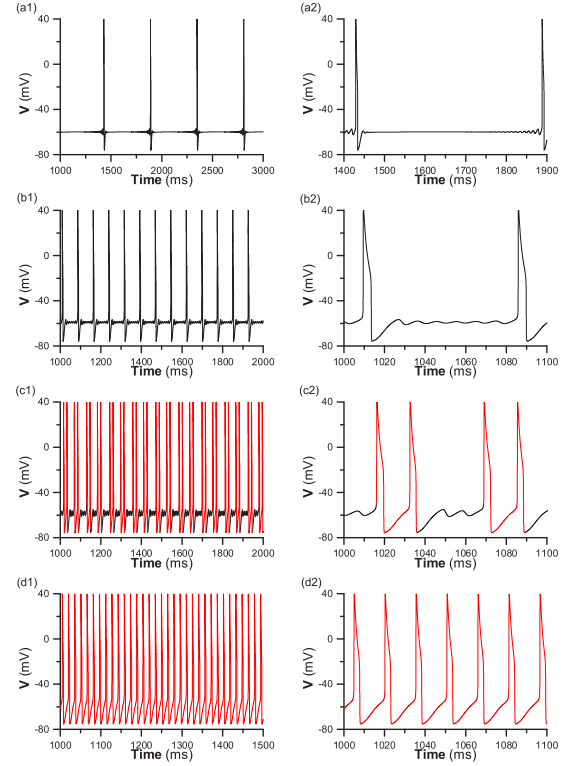


FIG. 2. Different firing patterns of the 3D deterministic HH neuron model when  $I_{app}$  is at different values. (a1, a2) MMOs of a single spike alternating with small amplitude oscillations when  $I_{app} = 9 \mu\text{A}/\text{cm}^2$ . (b1, b2) MMOs of a single spike alternating with small amplitude oscillations when  $I_{app} = 12 \mu\text{A}/\text{cm}^2$ . (c1, c2) MMOs of two successive spikes (red) alternating with small amplitude oscillations when  $I_{app} = 14.2 \mu\text{A}/\text{cm}^2$ . (d1, d2) Successive spiking (red) when  $I_{app} = 16 \mu\text{A}/\text{cm}^2$ . The right panels are partial enlargements of the left panels.

amplitude oscillations, as shown in Figs. 3(a1) and 3(a2). The ISIs of the MMOs are very large due to the large number of small amplitude oscillations, which indicates that the neuron fires slowly. When the noise amplitude is increased to  $D = 0.4 \mu\text{A}/\text{cm}^2$ , the firing pattern of the 3D HH neuron still is the class 1 MMOs, as shown in Figs. 3(b1) and 3(b2). However, the number of small amplitude oscillations is reduced, which results in the reduction of ISIs. When  $D = 0.6 \mu\text{A}/\text{cm}^2$ , the firing pattern of the 3D HH neuron becomes class 2 MMOs that are alternations of a spike, a cluster of spikes (a series of successive spiking, labeled with red), and multiple small amplitude oscillations, as shown in Figs. 3(c1) and 3(c2). Because of the further reduction of the number of small amplitude oscillations and the appearance of a cluster of spikes (successive spiking), the ISIs decrease further. As the noise amplitude is increased to  $D = 1.3 \mu\text{A}/\text{cm}^2$ , the firing pattern is still that of class 2 MMOs, but the successive spiking (red) appears more frequently [Figs. 3(d1) and 3(d2)], and the ISIs decrease further. When the noise amplitude is increased to  $D = 7 \mu\text{A}/\text{cm}^2$  [Figs. 3(e1) and 3(e2)] and  $D = 20 \mu\text{A}/\text{cm}^2$  [Figs. 3(f1) and 3(f2)], the firing pattern of the 3D HH neuron is changed to successive spiking. The ISIs become smaller. Compared to the above firing patterns, it can be found that

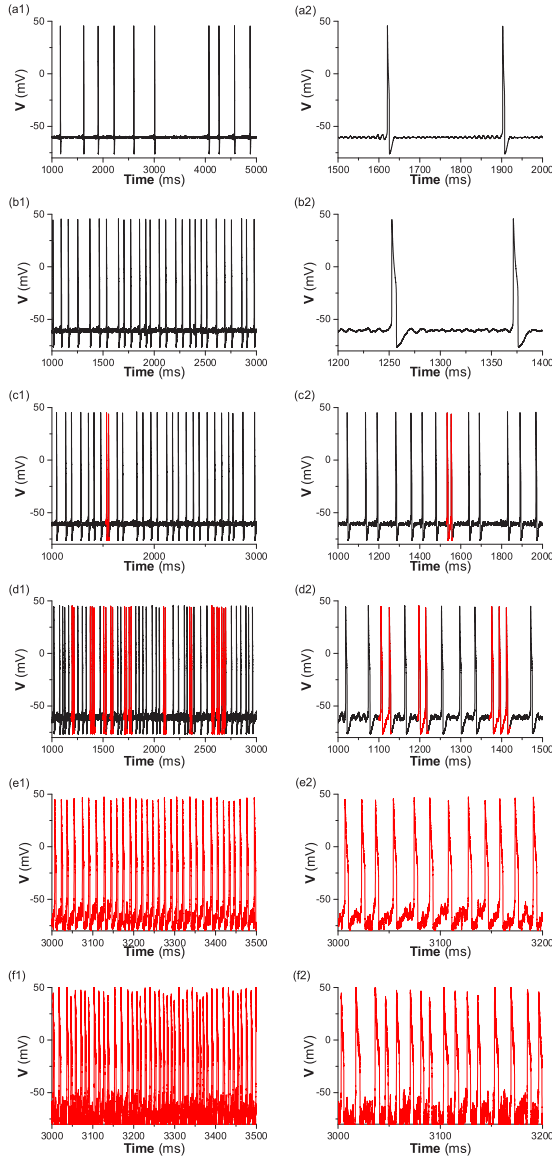


FIG. 3. Different firing patterns of the 3D stochastic HH neuron for different noise amplitude values. (a) Class 1 MMOs that are random alternations between a spike and multiple small amplitude oscillations when  $D = 0.1 \mu\text{A}/\text{cm}^2$ . (b) Class 1 MMOs when  $D = 0.4 \mu\text{A}/\text{cm}^2$ . (c) Class 2 MMOs that are random alternations of a spike, a cluster of spikes (red), and multiple small amplitude oscillations when  $D = 0.6 \mu\text{A}/\text{cm}^2$ . (d) Class 2 MMOs when  $D = 1.3 \mu\text{A}/\text{cm}^2$ . (e) Successive spiking (red) when  $D = 7 \mu\text{A}/\text{cm}^2$ . (f) Successive spiking (red) when  $D = 20 \mu\text{A}/\text{cm}^2$ .

the class 1 MMOs of a single spike alternating with multiple small amplitude oscillations have a larger ISI ( $>25$  ms), the successive spiking has a smaller ISI ( $<25$  ms), and the class 2 MMOs have both larger and smaller ISIs.

2. Noise induces different ISI distributions

ISIHs can be used to distinguish the characteristics of different firing patterns induced by noise. The probability density of the ISIs corresponding to Figs. 3(a)–3(f) is plotted, as

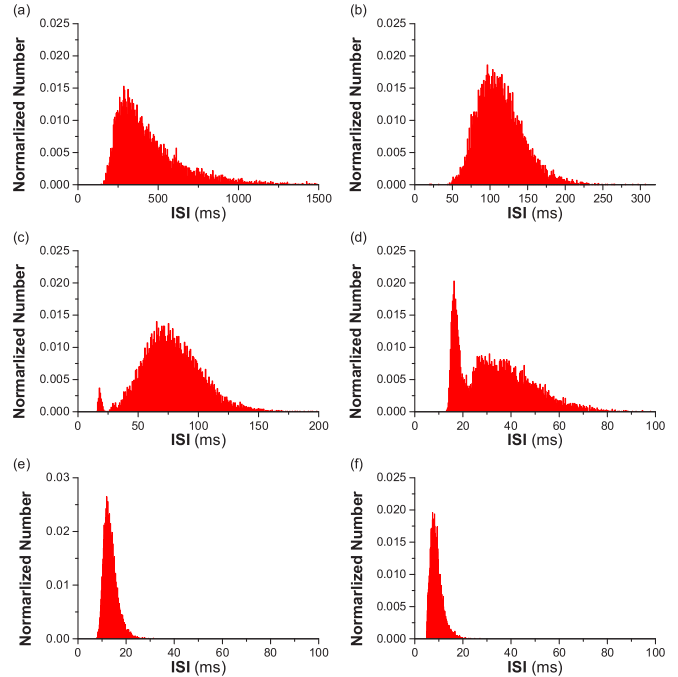


FIG. 4. ISIH of the 3D stochastic HH neuron for different values of the noise amplitude. (a)  $D = 0.1 \mu\text{A}/\text{cm}^2$ . (b)  $D = 0.4 \mu\text{A}/\text{cm}^2$ . (c)  $D = 0.6 \mu\text{A}/\text{cm}^2$ . (d)  $D = 1.3 \mu\text{A}/\text{cm}^2$ . (e)  $D = 7 \mu\text{A}/\text{cm}^2$ . (f)  $D = 20 \mu\text{A}/\text{cm}^2$ .

shown in Figs. 4(a)–4(f). When  $D = 0.1 \mu\text{A}/\text{cm}^2$ , the ISIH has a wide distribution, which corresponds to the larger ISIs of the class 1 MMOs [Fig. 3(a)], and the peak number (the number of ISIs in the peak of the ISIH) of the ISIs appears near 280 ms, as shown in Fig. 4(a). As the noise amplitude is increased to  $D = 0.4 \mu\text{A}/\text{cm}^2$ , the ISIH becomes narrower than that shown in Fig. 4(a), as shown in Fig. 4(b). However, the firing pattern is still that of class 1 MMOs [Fig. 3(b)]. The peak of the ISIs is decreased to  $\sim 105$  ms, and the peak number increases. When the noise amplitude is increased to  $D = 0.6 \mu\text{A}/\text{cm}^2$ , the firing pattern is changed to that of class 2 MMOs [Fig. 3(c)], and two peaks appear in the ISIH [Fig. 4(c)]. One peak corresponds to the successive spiking shown in Fig. 3(c), appears at  $\sim 19$  ms, and the ISIs have a narrow distribution. The other peak corresponding to the class 1 MMOs [Fig. 3(c)] appears at  $\sim 75$  ms, and the ISIs have a wide distribution. The peak number of ISIs corresponding to the wide distribution decreases. When the noise amplitude is increased to  $D = 1.3 \mu\text{A}/\text{cm}^2$ , the peak of the ISIs appears at  $\sim 18$  ms for the narrow distribution (corresponds to the successive spiking) and at  $\sim 27$  ms for the wide distribution (corresponding to the class 1 MMOs), as shown in Fig. 4(d). The peak number of ISIs for the narrow and wide distributions increases and decreases, respectively. When  $D = 7 \mu\text{A}/\text{cm}^2$ , the wide distribution (corresponding to the class 1 MMOs) disappears, and only the narrow distribution (corresponding to the successive spiking) exists, as shown in Fig. 4(e). The narrow distribution appears at  $\sim 13$  ms, and its peak number has a substantial increase. Upon further increasing, the noise amplitude becomes  $D = 20 \mu\text{A}/\text{cm}^2$ , the peak of the ISIs appears at  $\sim 8$  ms, and the peak number decreases.

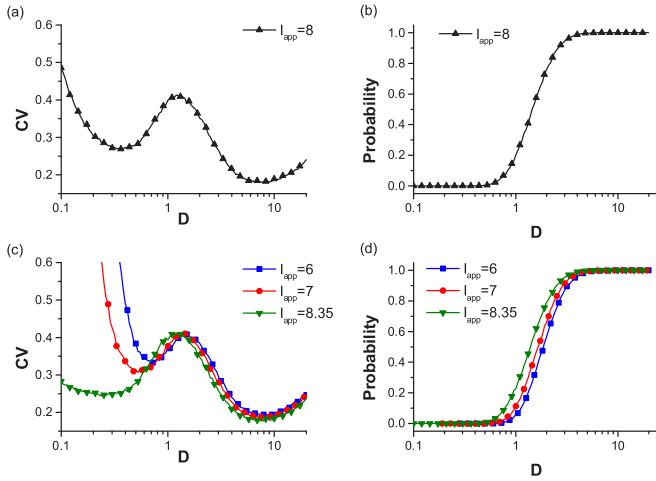


FIG. 5. Effects of the noise amplitude  $D$  on CV and probability of successive spiking when  $I_{app}$  is fixed at different values. (a) CV for  $I_{app} = 8 \mu\text{A}/\text{cm}^2$ . Two minima indicating DCRs appear. (b) Probability of successive spiking ( $\text{ISI} < 25 \text{ ms}$ ) for  $I_{app} = 8 \mu\text{A}/\text{cm}^2$ . (c) CVs for  $I_{app} = 6 \mu\text{A}/\text{cm}^2$ ,  $I_{app} = 7 \mu\text{A}/\text{cm}^2$ , and  $I_{app} = 8.35 \mu\text{A}/\text{cm}^2$ . (d) Probabilities of successive spiking ( $\text{ISI} < 25 \text{ ms}$ ) for  $I_{app} = 6 \mu\text{A}/\text{cm}^2$ ,  $I_{app} = 7 \mu\text{A}/\text{cm}^2$ , and  $I_{app} = 8.35 \mu\text{A}/\text{cm}^2$ .

Comparing all the wide distributions of ISIs in Figs. 4(a)–4(d), the intermediate noise amplitude ( $D = 0.4 \mu\text{A}/\text{cm}^2$ ) induces a local maximum of the peak number within the ISIs. The same comparison is performed for all the narrow distributions of the ISIs shown in Figs. 4(c)–4(f), the peak number of ISIs has a local maximum at a noise amplitude of  $D = 7 \mu\text{A}/\text{cm}^2$ . This indicates that white noise may induce DCRs.

### 3. Two minima of CV appear with the increase of noise amplitude

Figure 5(a) shows the changes of the CV as the noise amplitude  $D$  increases when  $I_{app} = 8 \mu\text{A}/\text{cm}^2$ . It is found that the value of CV decreases at first and then increases, and it then decreases and increases again, i.e., two local minima appear as the noise amplitude increases. This indicates that the CR appears twice, i.e., white noise can induce DCRs, which is different from the common result that a CR can be induced by white noise in single neuron models near a Hopf bifurcation [4,6,16,20,38].

During the first descending interval ( $0 < D < 0.4$ ), the firing pattern of the 3D HH neuron is that of class 1 MMOs that consist of a single spike alternating with multiple small amplitude oscillations [Figs. 3(a) and 3(b)]. With the increase of the noise amplitude, the number of small amplitude oscillations within each ISI decreases [Figs. 3(b) and 4(b)], which results in the drops of the time window of the subthreshold activity perturbed by white noise and the CV.

During the first increasing interval ( $0.4 < D < 1.2$ ), the firing pattern of the 3D HH neuron is changed to that of class 2 MMOs in which some successive spiking appears randomly. The random appearance of the successive spiking destroys the coherence of the class 1 MMOs [Fig. 3(c)]. With the increase of the noise amplitude, the probability of successive spiking

increases but is lower than 0.5 [Fig. 5(b)], which can lead to the increase of the CV.

For the second decreasing interval ( $1.2 < D < 7$ ), the firing pattern still is the class 2 MMOs, but successive spiking appears more frequently [the probability of successive spiking is larger than 0.5, Fig. 5(b)]. Since the time window perturbed by noise for successive spiking is smaller than that for the class 1 MMOs and the variability of ISIs for the successive spiking is smaller than that for the class 1 MMOs. Thus, the increase of the noise amplitude leads to the rise of probability of successive spiking and the decline of the CV. When the successive spiking accounts for the main parts of the firing pattern [probability of successive spiking is  $\sim 1$ , Fig. 5(b)], the CV reaches the local minimum [Fig. 5(a)].

For the second increasing interval ( $7 < D < 20$ ), although the firing pattern still is successive spiking, the noise amplitude in the interval is large, which can cause large fluctuations of the spike timing [Fig. 3(f)]. The fluctuations increase with the increase of the noise amplitude, which causes the increase of the CV.

When  $I_{app}$  is chosen from the other values in the interval of the resting state (stable equilibrium) located on the left of the SubH in Fig. 1, the noise amplitude  $D$  influences the CVs and the probabilities of successive spiking, as shown in Figs. 5(c) and 5(d), respectively. The results are the same as those for  $I_{app} = 8 \mu\text{A}/\text{cm}^2$  [Figs. 5(a) and 5(b)].

## C. Dynamical interpretations of the firing patterns induced by noise

The results described in the above subsection show that the appearance of DCRs depends on the changes of the firing patterns induced by white noise. In this part, the dynamical mechanism for the white-noise-induced different firing patterns is presented to study the generating mechanism of the white-noise-induced DCRs.

### 1. Trajectory evolution of the 3D deterministic HH model with different initial values

The steady-state behavior of the 3D deterministic HH neuron is the resting state that corresponds to the stable focus-node when  $I_{app} < I_H$ , but the transient behavior is different and is dependent on the initial values. For instance, at  $I_{app} = 8 \mu\text{A}/\text{cm}^2$ , when one of the initial values  $h$  is selected as 0.31, the membrane potentials for two different initial values [ $V(0) = -75, n(0) = 0.4$ ] and [ $V(0) = -75, n(0) = 0.45$ ], shown in Figs. 6(a) and 6(b), are changed into the resting potential (red line). However, the transient behaviors before the resting potential are different. One transient behavior is composed of small amplitude oscillations (blue line) with decreasing amplitude, as shown in Fig. 6(a), and the other is composed of a transient spike (green line) and small amplitude oscillations with increasing (black line) and decreasing amplitude (blue line), as shown in Fig. 6(b). The trajectories corresponding to Figs. 6(a) and 6(b) are plotted on the phase space ( $V, n, h$ ), as shown in Figs. 6(c) and 6(d), respectively. In Fig. 6(c), the trajectory is a spiral line (blue line) that converges to the stable focus-node (red solid circle) along the curve  $F^+$  (fold curve in the  $V$ -nullsurface), which

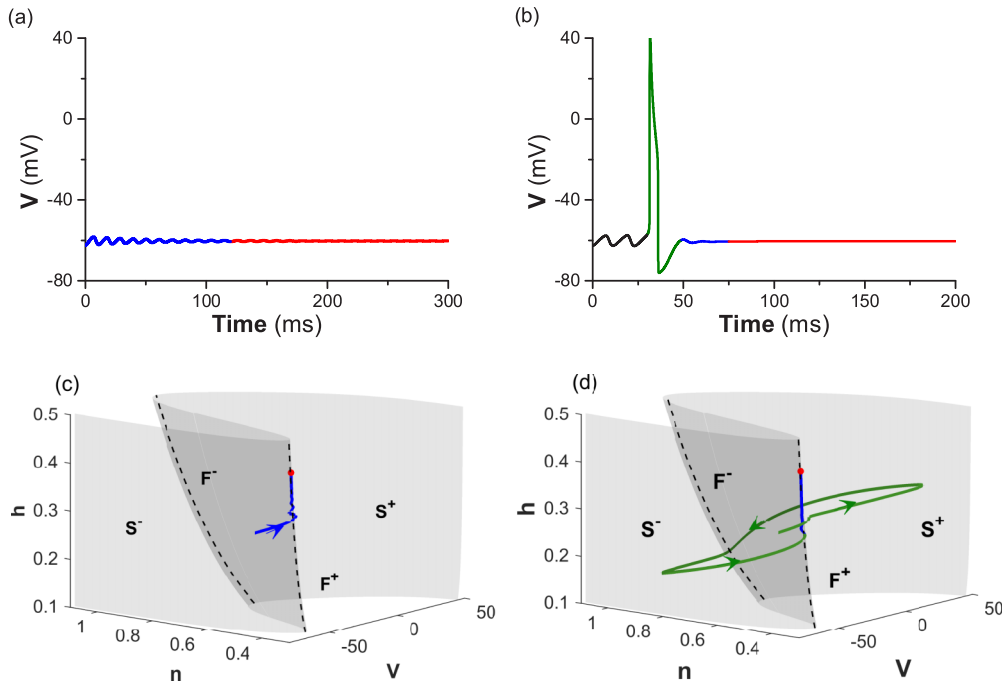


FIG. 6. Different transient behaviors of the 3D deterministic HH model with different initial values. (a) Transient behavior of small amplitude oscillations (blue line) with decreasing amplitudes before the resting state (red line) for initial values ( $V(0) = -75, n(0) = 0.45, h(0) = 0.31$ ). (b) Transient behavior composed of a spike (green line) and small amplitude oscillations with ascending (black line) and decreasing (blue line) amplitudes for initial values ( $V(0) = -75, n(0) = 0.4, h(0) = 0.31$ ). (c, d) Trajectories corresponding to panels (a, b) in the phase space ( $V, n, h$ ) with the same color scheme. The corresponding trajectories in the phase space ( $V, n, h$ ) have the same color scheme as the membrane potentials in panels (a, b). The gray cubic-shaped surface is the  $V$ -nullsurface,  $S^-$  and  $S^+$  are left and right attracting sheets of the  $V$ -nullsurface, and the black dashed curves  $F^-$  and  $F^+$  are the fold curve in the  $V$ -nullsurface. The red solid circle is the stable focus-node.

corresponds to the generation of the small amplitude oscillations with decreasing amplitude [Fig. 6(a)]. In Fig. 6(d), the trajectories move from the initial point (corresponding initial values) toward the right branch  $S^+$  (attracting sheet) of the  $V$ -nullsurface, and then along  $S^+$  toward the left curve  $F^-$  (fold curve in the  $V$ -nullsurface), switch to the left branch  $S^-$  (attracting sheet) of the  $V$ -nullsurface and along branch  $S^-$  toward the right curve  $F^+$ . When the trajectories reach the neighborhood of  $F^+$ , the trajectories spiral slowly to the stable focus-node along  $F^+$  due to that  $F^+$  is almost parallel to the  $h$  axis and  $h$  is the slow variable. Thus, the amplitude of the membrane potential first increases to form a spike and then decreases to form small amplitude oscillations with a decreasing amplitude and with a resting state [Fig. 6(b)].

## 2. Separatrix surface of action potential in phase space

Transient behaviors can be used to reveal the relevant features of systems and the dynamical behaviors of systems subjected to external forces [62–66]. For example, the noise-induced chaos can be explained based on the transient chaos of systems [62–64]. This subsection describes how the separatrix surface of the spiking and subthreshold oscillations in the phase space ( $V, n, h$ ) is obtained based on the transient behaviors from different initial values. This is used to explain the changes in the firing patterns induced by noise.

The distinct transient behaviors (Fig. 6) depend on the choice of the initial values. There is a separatrix curve (sur-

face) that separates the phase plane ( $V, n$ ) [the phase space ( $V, n, h$ )] into two regions of initial values that evolve into the two different transient behaviors. The separatrix curve (surface) can be regarded as the threshold of the action potential [67]. It should be noted that the transient behavior is considered a transient spike when the membrane potential crosses over 0 mV. To present the effects of the separatrix curve (surface), a separatrix curve [67,68] (magenta solid curve) that separates the phase plane ( $V, n$ ) into two different transient behaviors and the phase trajectories corresponding to Figs. 6(a) and 6(b) are plotted in the phase plane ( $V, n$ ) when  $h = 0.31$ , as shown in Figs. 7(a) and 7(b). When the initial values are chosen from the outside of the separatrix curve [Fig. 7(b)], the transient behavior has spiking [Fig. 6(b)]. Otherwise [Fig. 7(a)], no transient spiking appears [Fig. 6(a)]. To present the effect of the initial values of the variables ( $V, n, h$ ) on the transient behavior, the separatrix surface (magenta) and the trajectory corresponding to Figs. 6(a) and 6(b) are plotted in phase space ( $V, n, h$ ), as shown in Figs. 7(c) and 7(d). The separatrix curve in Figs. 7(a) and 7(b) is the intersection of the separatrix surface in Figs. 7(c) and 7(d) with a plane  $h = 0.31$ . If the initial values are chosen from the bottom of the separatrix surface, then the trajectory spins into the stable focus-node directly [Fig. 7(c)]. Otherwise, the trajectory moves to the top right of the phase space to form a spike [Figs. 7(d) and 6(b)]. Later, the trajectory moves to the area below the separatrix surface and spins into the stable focus-node to form small amplitude oscillations.

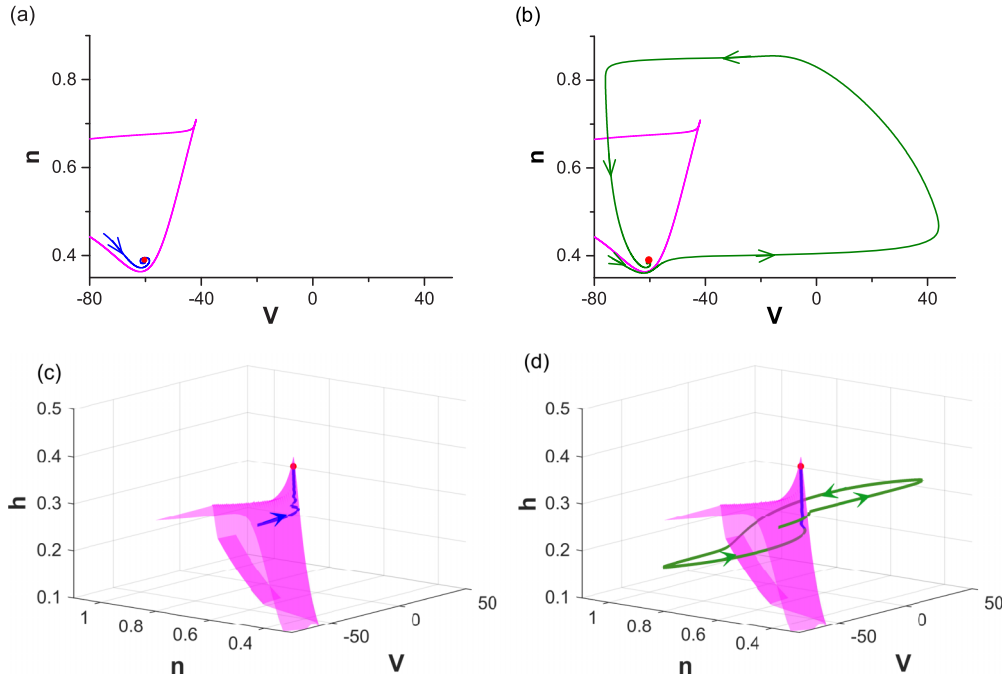


FIG. 7. Separatrix curve (surface) of action potential. (a) Trajectory of small amplitude oscillations projected upon  $(V, n)$  when initial values lie inside of the separatrix curve (magenta). (b) Trajectory of transient spike and small amplitude oscillations projected upon  $(V, n)$  when initial values lie outside of the separatrix curve. (c) Trajectory of small amplitude oscillations in phase space  $(V, n, h)$  when initial values lie under the separatrix surface (magenta). (d) Trajectory of transient spike and small amplitude oscillations in phase space  $(V, n, h)$  when initial values are above the separatrix surface (magenta). The initial values for (a) and (c) [(b) and (d)] are the same as in Fig. 6(a) [Fig. 6(b)].

### 3. Noise-induced changes of trajectory in phase space

In this subsection, we describe the analysis of the dynamical mechanism of different firing patterns induced by the white noise. The trajectories corresponding to Figs. 3(a)–3(e) are plotted in the phase space  $(V, n, h)$ , as shown in Figs. 8(a)–8(e), respectively. With the perturbations of small noise amplitude ( $D = 0.1 \mu\text{A}/\text{cm}^2$ ), the trajectory rotates around the stable focus-node many times anticlockwise and may easily cross over the convex part of the separatrix surface near the stable focus (red solid circle) from inside to outside due to the close spatial distance between the stable focus-node and the convex part in the phase space, as shown in Fig. 8(a). If the trajectory has crossed over the convex part, then the trajectory may rotate away from the convex part anticlockwise to the upper right corner to form a spike. Then, the trajectory will move to the area below the convex part and spin into the stable focus-node. Consequently, class 1 MMOs that are composed of a spike and multiple small amplitude oscillations are formed [Fig. 3(a)]. When the noise amplitude is increased to  $D = 0.4 \mu\text{A}/\text{cm}^2$  [Fig. 8(b)], it becomes relatively easier for the trajectory to cross over the convex part, and the range of the trajectory that can cross over the convex part is enlarged, which can result in the reduction of the trajectory rotating around the stable focus-node, i.e., the rotation number of small amplitude oscillations decreases [Fig. 3(b)]. When the noise amplitude is increased to  $D = 0.6 \mu\text{A}/\text{cm}^2$ , some trajectories (marked in red) will not spin into the region near the convex part around the stable focus-node, but they will cross over the remaining part of the separatrix surface

in addition to the convex part, as shown in Fig. 8(c). Thus, there are no small amplitude oscillations within two adjacent spikes [Fig. 3(c)], i.e., successive spiking appears randomly and class 2 MMOs are evoked. With the increase of the noise amplitude, for instance,  $D = 1.3 \mu\text{A}/\text{cm}^2$ , there is a larger probability of trajectory that can cross over the remaining parts of the separatrix rather than the convex part [Fig. 8(d)], i.e., successive spiking appears more frequently [Fig. 3(d)]. With the further increase of the noise amplitude, for instance,  $D = 7 \mu\text{A}/\text{cm}^2$ , the trajectory rarely enters into the regions surrounded by the convex part but can easily cross over the remaining part of the separatrix surface rather than the convex part [Fig. 8(e)], i.e., the firing pattern is changed to successive spiking [Fig. 3(e)]. When the noise amplitude is increased to  $D = 20 \mu\text{A}/\text{cm}^2$  [Fig. 8(f)], although the firing pattern is still successive spiking, the trajectory becomes irregular due to the great fluctuations aroused by the strong noise amplitude.

### 4. Dependence of the two coherent firing patterns on variable $h$

From Fig. 8, it can be seen that the firing patterns aroused by different noise amplitudes depend on the values  $h$  at which the trajectories cross the separatrix surface. To clearly present the effects of  $h$  on the generation of two firing patterns, the trajectories corresponding to Figs. 8(b) and 8(e) in phase space  $(V, n, h)$  with  $V$ -nullsurface are plotted, as shown in Figs. 9(a) and 9(b).

Comparing the trajectories in Figs. 9(a) and 9(b), it can be seen that the difference between the two firing patterns



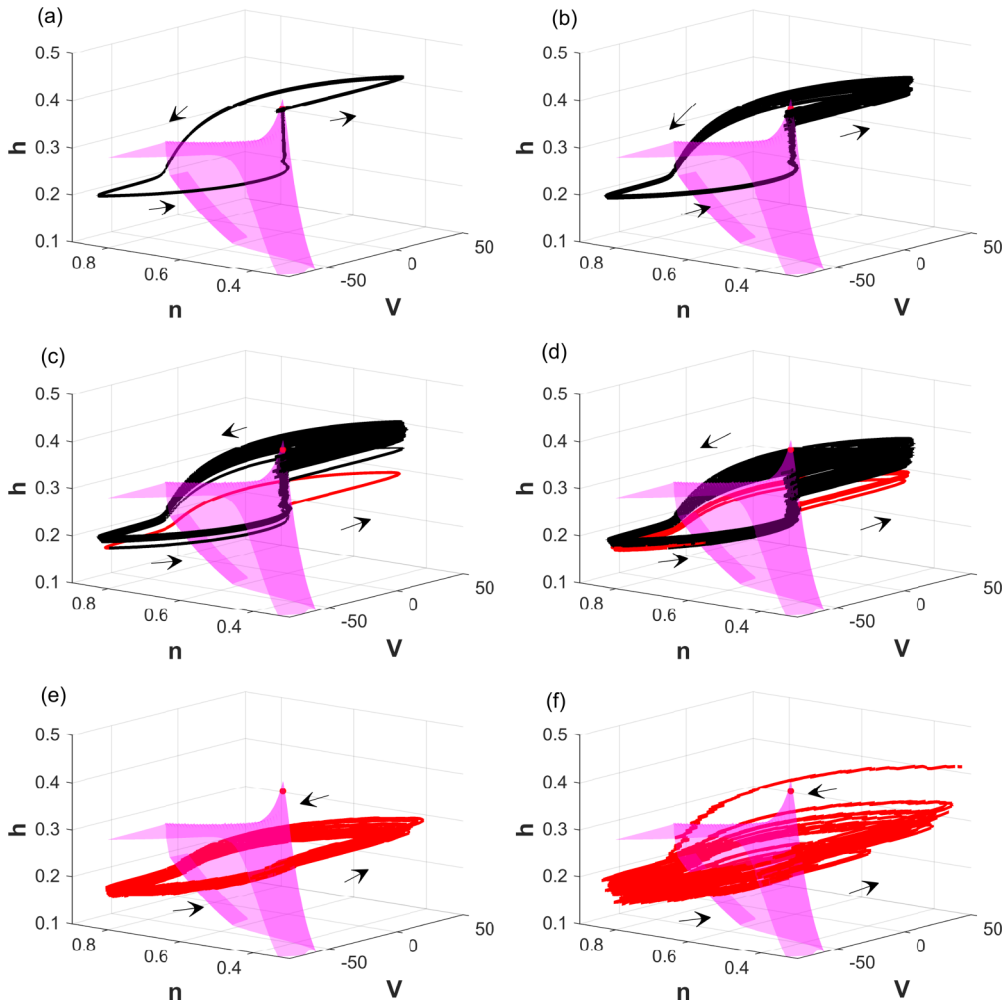


FIG. 8. Trajectories in the phase space  $(V, n, h)$  for different noise amplitudes. (a)  $D = 0.1 \mu\text{A}/\text{cm}^2$ . (b)  $D = 0.4 \mu\text{A}/\text{cm}^2$ . (c)  $D = 0.6 \mu\text{A}/\text{cm}^2$ . (d)  $D = 1.3 \mu\text{A}/\text{cm}^2$ . (e)  $D = 7 \mu\text{A}/\text{cm}^2$ . (f)  $D = 20 \mu\text{A}/\text{cm}^2$ . The black and red lines are the trajectories of the MMOs and successive spiking, respectively. The red solid circle is the stable focus-node. The magenta surface is the separatrix surface of the action potential (threshold of action potential). The directions of the trajectories are indicated by the arrows.

of the class 1 MMOs [Fig. 9(a)] and the successive spiking [Fig. 9(b)] is determined by whether or not the trajectories can spiral toward the stable focus-node along  $F^+$  to form small amplitude oscillations. The  $V$ -nullsurface is a cubic-shaped surface and the fold curve  $F^+$  is almost parallel to the  $h$

axis. With the perturbation of noise with small amplitude, the trajectories spiral slowly toward the focus-node along  $F^+$  due to the slow varying of  $h$  and the stable focus-node, and then cross the convex part of the separatrix surface (near  $h = 0.4$ ) [Fig. 9(b)] and toward the right branch  $S^+$ , which results in

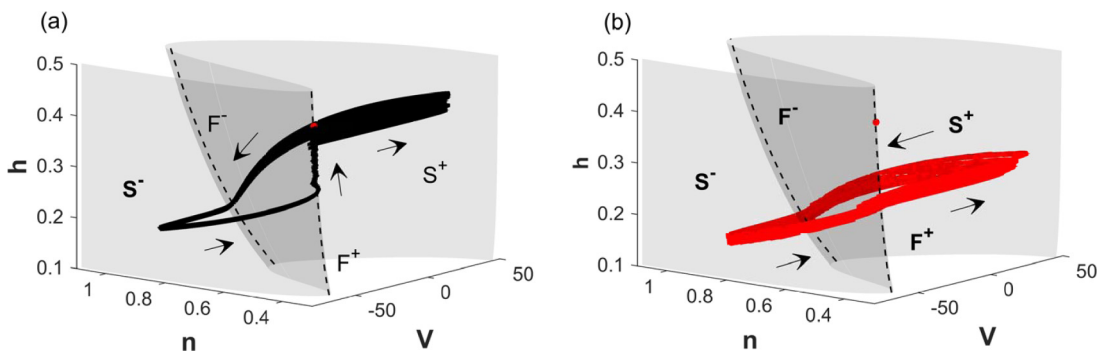


FIG. 9. Comparison between the trajectories of the class 1 MMOs and the successive spiking in the phase space  $(V, n, h)$ . (a) The trajectory of the class 1 MMOs. (b) The trajectory of the successive spiking.

multiple small amplitude oscillations followed by a spike; i.e., the class 1 MMOs depend on the slow varying of  $h$  and the larger value  $h$  at which trajectory cross the separatrix surface, as shown in Fig. 9(a). The generation of the MMOs is similar to the canard-induced MMOs in deterministic neuron models that have two slow variables [55]. With the perturbation of noise with large amplitude, the trajectories can cross the separatrix surface (near  $h = 0.28$ ) without spiraling toward the focus-node along  $F^+$  [Fig. 9(e)]; i.e., for the successive spiking, the trajectories cross the separatrix surface at lower value  $h$  and there is no slow varying of  $h$ .

#### IV. DISCUSSIONS AND CONCLUSIONS

Noise plays constructive roles in the generation of CR, which is one of the most famous phenomena. Usually, single CR is aroused by white noise from the resting state near a Hopf bifurcation. In this research, DCRs induced by white noise are found near the subcritical Hopf bifurcation in the 3D HH neuron model, and the dynamical mechanism is revealed. The multiple-timescale feature of the 3D model is the key to the generation of DCRs, based on which the phenomenon can be generalized to 4D models.

The appearance of DCRs is related to the firing patterns induced by noise, which depend on the intrinsic dynamical characteristics of the 3D HH neuron model. Under the influence of the weak noise, the trajectory rotating around the stable focus-node crosses over the convexity of the threshold surface. Then, the trajectory rotates away from the convexity to form a spike. During the whole process, multiple small amplitude oscillations followed by a spike are formed, i.e., class 1 MMOs are induced by the noise. When the noise amplitude increases, the ISIs decrease, which causes the firing pattern of the class 1 MMOs to be more regular. When the noise amplitude is increased to a certain value, some trajectories far away from the stable focus-node can cross over the threshold surface far away from the stable focus-node to form successive spikes without rotating around the stable focus-node, i.e., successive spiking appears randomly with the class 1 MMOs. The random appearance of successive spiking destroys the regularity of the firing pattern of the class 1 MMOs. Thus, the CV decreases at first and then increases as the noise amplitude increases, i.e., the optimal coherence of the firing pattern of the class 1 MMOs appears with the first CR. With the further increase of the noise amplitude, the proportion of the successive spiking is more than half of all the firing pattern, and its ratio increases, which causes the CV to decrease. When the successive spiking plays a prominent role, a suitable noise amplitude can optimize the firing responses and cause the CV to achieve a local minimum. When the noise amplitude is larger than the suitable noise amplitude, the fluctuations of the trajectory become large as the noise amplitude increases, which causes great fluctuations of the spike timing and increases of the CV, i.e., the optimal coherence of the firing pattern of the successive spiking appears with the second CR. Based on the above discussion, the changes of the firing pattern aroused by the white noise play critical roles in the appearance of DCRs. The firing patterns induced by the noise depend on the slow variable  $h$  and the inverse U-shaped separatrix surface (Figs. 8 and 9). That is, the DCRs

depend on the multiple-timescale feature and the shape of the separatrix surface of the 3D HH neuron model. In addition, the noise-induced firing patterns (Fig. 3) are similar to the firing patterns of the 3D deterministic HH model induced by the applied current (Fig. 2), which is due to the noisy precursors of the bifurcations [38]. However, the generation of MMOs in the deterministic 3D HH neuron model also depends on the multiple-timescale feature, i.e., the generation of the MMOs requires that the phase space of the deterministic model has at least three dimensions. The 3D deterministic HH model has a fast variable and two slow variables, and the model can exhibit MMOs and successive spiking, which is different from the two-dimensional neuron models (continuous systems) that have a slow variable and a fast variable such as the Morris–Lecar [18] and FitzHugh–Nagumo neuron models [4,6,20,38,69]. The difference in timescales between the 3D HH neuron model and these two-dimensional neuron models can arouse the different firing patterns not only in deterministic models but also in stochastic models [69]; that is, the white noise has different effects on the CR for the 3D HH neuron model and two-dimensional neuron models. Thus, it may be difficult to extend the result of this research to these two-dimensional neuron models.

The result that white noise can induce DCRs is different from previous findings about DCRs or multiple CRs. A previous study [45] showed that the white noise can induce DCRs in the Rulkov model, which is a discrete system, and the underlying mechanism was unclear. In this study, the 3D HH neuron model is a continuous system, and the underlying mechanism for the DCRs is interpreted according to the changes of the firing pattern induced by noise. There are many differences in the dynamics of these two systems. In addition, some studies [17,21,35,51–53] have shown that multiple CRs appear as time delay in the coupling term increases, where time delay, rather than noise, induces multiple CRs. The reason that time delay induces multiple CRs is that the entrainment of the period of noise-induced motion by time delay, which is different from the noise-induced DCRs in this study. Recent studies [42–44] have shown phase-noise-induced DCRs in a FitzHugh–Nagumo neuron (corresponding to Hopf bifurcation), in which one CR occurs at the average frequency of the phase noise and the other one occurs at the intrinsic firing frequency of the FitzHugh–Nagumo neuron, i.e., the generation of the DCRs depends on the frequency characteristic of the phase noise. However, the white noise used in the study does not have the frequency characteristic. In this study, the occurrence of DCRs depends on the multiple-timescale feature of the 3D HH neuron model. Previous studies showed doubly stochastic coherence induced by white noise [46,48]. In these studies, the appearance of doubly stochastic coherence is the joint effect of additive noise and multiplicative noise, i.e., there are two sources of noise present simultaneously. In this paper, the generation of the DCRs only requires additive noise.

The result described in this paper presents a particular case in which white noise can induce DCRs rather than single CR from the resting state near the subcritical Hopf bifurcation. The appearance of DCRs depends on the intrinsic dynamical characteristics of the 3D HH neuron model that has a fast variable and two slow variables, i.e., the multiple-

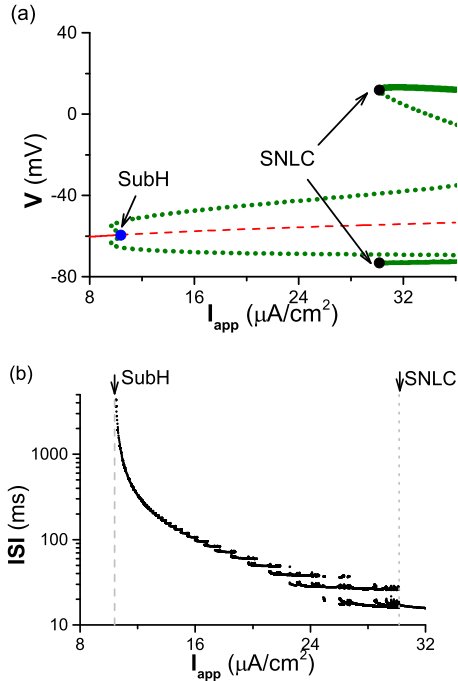


FIG. 10. Bifurcation diagram of the 4D deterministic HH model with the increase of  $I_{app}$ . (a) Bifurcations of equilibrium (red) and limit cycle (green). The red solid and dashed curves denote the stable and unstable equilibria, respectively. The green solid and dotted curves denote the maximum and minimum values of the stable and unstable limit cycles, respectively. The blue and black solid circles denote the bifurcation points SubH and SNLC, respectively. (b) Other complex bifurcations of limit cycle when  $I_{app}$  is located between SubH and SNLC.

timescale feature of the 3D HH neuron model. In this paper, the model that white noise is introduced to the equation of membrane potential is analyzed, when Gaussian stochastic process is introduced into the equations of the gating variables, there are similar results (not given in this paper) due to the multiple-timescale feature. Since noise is ubiquitous in nervous systems [1,5], the research presents one case in which neurons may utilize noise to enhance information processing and transformation, which are helpful for understanding the role of noise in neuronal systems with multiple-timescale feature.

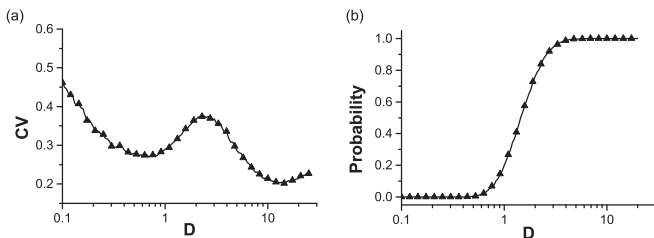


FIG. 11. Effects of the noise amplitude  $D$  on CV and probability of successive spiking for the 4D HH neuron model when  $I_{app} = 10.3 \mu A/cm^2$ . (a) CV. Two minima indicate the appearance of DCRs. (b) Probability of successive spiking ( $ISI < 25$  ms).

ACKNOWLEDGMENTS

This work was supported by the Science and Technology Project of Guangzhou (Grant No. 202102021167), GDAS' Project of Science and Technology Development (Grant No. 2021GDASYL-20210103088), the National Natural Science Foundation of China (Grant No. 11802085), and the Science and Technology Development Program of Henan Province (Grant No. 212102310827).

APPENDIX: RESULTS FOR THE 4D HH NEURON MODEL

In this Appendix, some results that the influences of the white noise on the 4D HH neuron model being composed by Eqs. (2)–(4) and (8), are presented.

1. Dynamical behaviors for the 4D deterministic HH neuron

For the 4D deterministic HH neuron model, the bifurcation diagram of the membrane potential with respect to  $I_{app}$  is shown in Fig. 10(a). There is a unique equilibrium (red curve) even for a larger range of  $I_{app}$ . With the increase of  $I_{app}$ , the stable equilibrium (red solid curve) changes to the unstable equilibrium (red dashed curve) via subcritical Hopf bifurcation (SubH, blue solid circle) at  $I_H := I_{app} \approx 10.3859 \mu A/cm^2$ . A branch of unstable limit cycles (green dashed curve) is bifurcated from the Hopf bifurcation point SubH. The unstable limit cycle bifurcated from Hopf bifurcation collides with the stable limit cycle (green solid curve) at the point  $I_{app} \approx 30.1643 \mu A/cm^2$  (black solid circles), which is a saddle-node bifurcation of the limit cycles (SNLC).

Some complex bifurcations and dynamical behaviors are found in the interval between the bifurcation points SubH and SNLC. The changes of the ISIs with respect to  $I_{app}$  are shown in Fig. 10(b). When  $10.3859 \mu A/cm^2 < I_{app} < 26.02 \mu A/cm^2$ , the dynamical behavior is single spike alternating with multiple small amplitude oscillations, i.e., MMOs. With the increase of  $I_{app}$ , the number of small amplitude oscillations decreases, which results in the decrease of the ISIs [Fig. 10(b)]. When  $26.02 \mu A/cm^2 < I_{app} < 30.1643 \mu A/cm^2$ , the firing pattern is still MMOs, however, the MMOs are a cluster of successive spikes alternating with multiple small amplitude oscillations.

2. White-noise-induced DCRs

When  $I_{app} = 10.3 \mu A/cm^2$ , the 4D deterministic HH neuron model is at resting state. CV and probability of successive spiking with respect to the noise amplitude  $D$  are shown in Figs. 11(a) and 11(b), respectively.

3. Noise-induced firing patterns and their trajectories

When  $D = 0.7 \mu A/cm^2$  and  $D = 14 \mu A/cm^2$  [two minima in Fig. 11(a)], the firing patterns are class 1 MMOs [Fig. 12(a)] and the successive spiking [Fig. 12(b)], respectively. To better explain the firing patterns, the corresponding trajectories in phase space ( $V, n, h$ ) are shown in Figs. 12(c) and 12(d), respectively. The evolution of the trajectories is

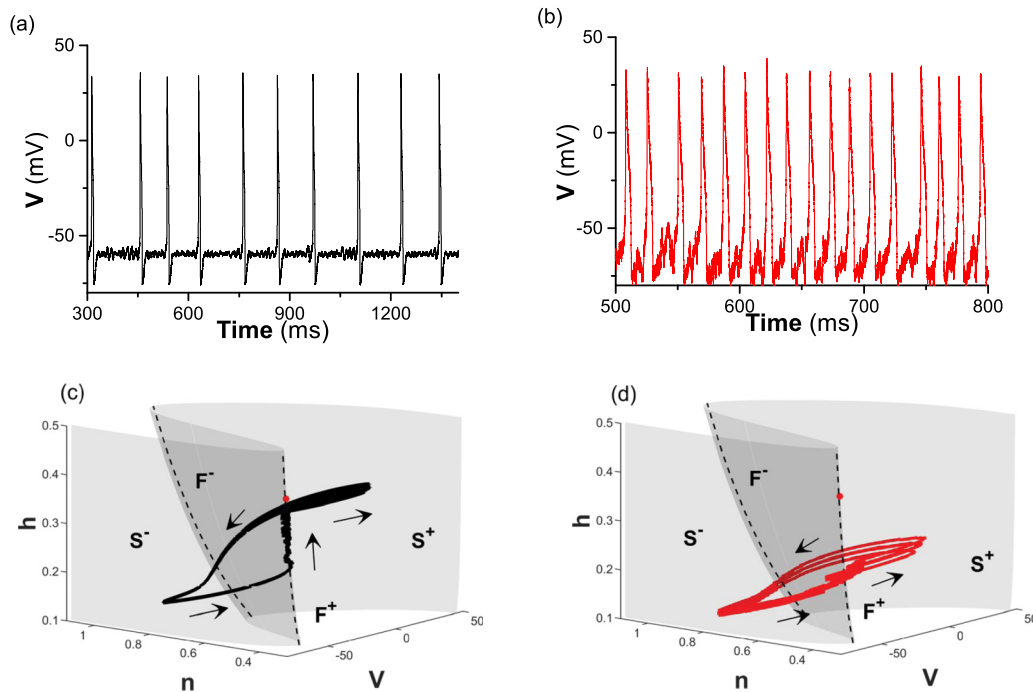


FIG. 12. Comparison between the firing patterns and trajectories of the 4D HH neuron model when  $D = 0.7 \mu\text{A}/\text{cm}^2$  and  $D = 14 \mu\text{A}/\text{cm}^2$ . (a) Class 1 MMOs when  $D = 0.7 \mu\text{A}/\text{cm}^2$ . (b) Successive spiking when  $D = 14 \mu\text{A}/\text{cm}^2$ . (c) The trajectory of the class 1 MMOs. (d) The trajectory of the successive spiking.

also the same as that of the 3D HH neuron model [Figs. 9(a) and 9(b)]. Thus, the mechanism of the white-noise-induced

DCRs for the 4D HH neuron model is the same as this for the 3D HH neuron model.

- [1] A. A. Faisal, L. P. J. Selen, and D. M. Wolpert, *Nat. Rev. Neurosci.* **9**, 292 (2008).
- [2] L. Gamaitoni, P. Hänggi, P. Jung, and F. Marchesoni, *Rev. Mod. Phys.* **70**, 223 (1998).
- [3] H. Gang, T. Ditzinger, C. Z. Ning, and H. Haken, *Phys. Rev. Lett.* **71**, 807 (1993).
- [4] A. S. Pikovsky and J. Kurths, *Phys. Rev. Lett.* **78**, 775 (1997).
- [5] M. D. McDonnell and D. Abbott, *PLoS Comput. Biol.* **5**, e1000348 (2009).
- [6] O. V. Ushakov, H. J. Wunsche, F. Henneberger, I. A. Khovanov, L. Schimansky-Geier, and M. A. Zaks, *Phys. Rev. Lett.* **95**, 123903 (2005).
- [7] Y. Kato and H. Nakao, *New J. Phys.* **23**, 043018 (2021).
- [8] K. Miyakawa and H. Isikawa, *Phys. Rev. E* **66**, 046204 (2002).
- [9] X. Y. Li, D. Zhao, and B. L. Shi, *J. Acoust. Soc. Am.* **145**, 692 (2019).
- [10] J. E. Levin and J. P. Miller, *Nature (London)* **380**, 165 (1996).
- [11] P. Cordo, J. T. Inglis, S. Verschueren, J. J. Collins, D. M. Merfeld, S. Rosenblum, S. Buckley, and F. Moss, *Nature (London)* **383**, 769 (1996).
- [12] A. N. Pisarchik, V. A. Maksimenko, A. V. Andreev, N. S. Frolov, V. V. Makarov, M. O. Zhuravlev, A. E. Runnova, and A. E. Hramov, *Sci. Rep.* **9**, 18325 (2019).
- [13] C. Trenado, I. Mendez-Balbuena, E. Manjarrez, F. Huehe, J. Schulte-Menting, B. Feige, M. C. Hepp-Reymond, and R. Kristeva, *Front. Hum. Neurosci.* **8**, 325 (2014).
- [14] J. J. Collins, T. T. Imhoff, and P. Grigg, *J. Neurophysiol.* **76**, 642 (1996).
- [15] M. Wuehr, J. C. Boerner, C. Pradhan, J. Decker, K. Jahn, T. Brandt, and R. Schniepp, *Brain Stimul.* **11**, 261 (2018).
- [16] S. G. Lee, A. Neiman, and S. Kim, *Phys. Rev. E* **57**, 3292 (1998).
- [17] X. L. Song, H. T. Wang, and Y. Chen, *Nonlinear Dyn.* **94**, 141 (2018).
- [18] R. Guantes and G. G. de Polavieja, *Phys. Rev. E* **71**, 011911 (2005).
- [19] Y. Xu, L. L. Lu, M. Y. Ge, and Y. Jia, *Eur. Phys. J. B* **95**, 245 (2019).
- [20] R. E. Lee DeVile, E. Vanden-Eijnden, and C. B. Muratov, *Phys. Rev. E* **72**, 031105 (2005).
- [21] N. B. Janson, A. G. Balanov, and E. Schöll, *Phys. Rev. Lett.* **93**, 010601 (2004).
- [22] Y. Horikawa, *Phys. Rev. E* **64**, 031905 (2001).
- [23] A. Longtin, *Phys. Rev. E* **55**, 868 (1997).
- [24] A. Longtin and K. Hinzer, *Neural Comput.* **8**, 215 (1996).
- [25] B. Cao, R. X. Wang, H. G. Gu, and Y. Y. Li, *Cognit. Neurodynam.* **15**, 77 (2021).
- [26] H. G. Gu, M. H. Yang, L. Li, Z. Q. Liu, and W. Ren, *NeuroReport* **13**, 1657 (2002).
- [27] S. G. Wu, W. Ren, K. F. He, and Z. Q. Huang, *Phys. Lett. A* **279**, 347 (2001).
- [28] D. Q. Guo and C. G. Li, *Phys. Rev. E* **79**, 051921 (2009).

- [29] R. Tönjes, C. E. Fiore, and T. Pereira, *Nat. Commun.* **12**, 72 (2021).
- [30] M. E. Yamakou and J. Jost, *Phys. Rev. E* **100**, 022313 (2019).
- [31] M. Masoliver, C. Masoller, and A. Zakharova, *Chaos, Solitons Fractals* **145**, 110666 (2021).
- [32] M. E. Yamakou, P. G. Hjorth, and E. A. Martens, *Front. Comput. Neurosci.* **14**, 62 (2020).
- [33] M. Masoliver, N. Malik, E. Schöll, and A. Zakharova, *Chaos* **27**, 101102 (2017).
- [34] C. S. Zhou, J. Kurths, and B. Hu, *Phys. Rev. Lett.* **87**, 098101 (2001).
- [35] Q. Y. Wang, M. Perc, Z. S. Duan, and G. R. Chen, *Chaos* **19**, 023112 (2009).
- [36] H. T. Yu, J. Wang, J. W. Du, B. Deng, X. L. Wei, and C. Liu, *Phys. Rev. E* **87**, 052917 (2013).
- [37] M. Perc, *Phys. Rev. E* **72**, 016207 (2005).
- [38] A. Neiman, P. I. Saparin, and L. Stone, *Phys. Rev. E* **56**, 270 (1997).
- [39] B. Jia, H. G. Gu, and Y. Y. Li, *Chin. Phys. Lett.* **28**, 090507 (2011).
- [40] H. G. Gu, H. M. Zhang, C. L. Wei, M. H. Yang, Z. Q. Liu, and W. Ren, *Int. J. Mod. Phys. B* **25**, 3977 (2011).
- [41] R. Aust, P. Hövel, J. Hizanidis, and E. Schöll, *Eur. Phys. J.: Spec. Top.* **187**, 77 (2010).
- [42] Y. B. Jia and H. G. Gu, *Chaos* **25**, 123124 (2015).
- [43] X. M. Liang, L. Zhao, and Z. H. Liu, *Phys. Rev. E* **84**, 031916 (2011).
- [44] X. M. Liang, M. Dhamala, L. Zhao, and Z. H. Liu, *Phys. Rev. E* **82**, 010902(R) (2010).
- [45] Y. Jiang, *Phys. Rev. E* **71**, 057103 (2005).
- [46] A. Zaikin, J. García-Ojalvo, R. Bascones, E. Ullner, and J. Kurths, *Phys. Rev. Lett.* **90**, 030601 (2003).
- [47] B. Lindner, J. García-Ojalvo, A. Neimand, and L. Schimansky-Geiere, *Phys. Rep.* **392**, 321 (2004).
- [48] Y. Gao and J. J. Wang, *Phys. Rev. E* **86**, 051914 (2012).
- [49] T. Kreuz, S. Luccioli, and A. Torcini, *Phys. Rev. Lett.* **97**, 238101 (2006).
- [50] X. J. Sun, M. Perc, Q. S. Lu, and J. Kurths, *Chaos* **18**, 023102 (2008).
- [51] Q. Y. Wang, H. H. Zhang, M. Perc, and G. R. Chen, *Commun. Nonlinear Sci. Numer. Simul.* **17**, 3979 (2012).
- [52] E. Yilmaz, M. Ozer, V. Baysal, and M. Perc, *Sci. Rep.* **6**, 30914 (2016).
- [53] X. Lin, Y. B. Gong, and L. Wang, *Chaos* **21**, 043109 (2011).
- [54] C. Men, J. Wang, Y. M. Qin, B. Deng, K. M. Tsang, and W. L. Chan, *Chaos* **22**, 013104 (2012).
- [55] M. Desroches, J. Guckenheimer, B. Krauskopf, C. Kuehn, H. M. Osinga, and M. Wechselberger, *SIAM Rev.* **54**, 211 (2012).
- [56] J. Rubin and M. Wechselberger, *Biol. Cybern.* **97**, 5 (2007).
- [57] B. Ermentrout, *Simulating, Analyzing, and Animating Dynamical Systems: A Guide to XPPAUT for Researchers and Students* (SIAM, Philadelphia, PA, 2002), p. 12.
- [58] D. J. Higham, *SIAM Rev.* **43**, 525 (2001).
- [59] B. Lindner, A. Longtin, and A. Bulsara, *Neural Comput.* **15**, 1761 (2003).
- [60] J. W. Shuai, S. Zeng, and P. Jung, *Fluctuation Noise Lett.* **2**, L139 (2002).
- [61] J. W. Shuai and P. Jung, *Phys. Rev. Lett.* **88**, 068102 (2002).
- [62] Y. C. Lai, Z. H. Liu, L. Billings, and I. B. Schwartz, *Phys. Rev. E* **67**, 026210 (2003).
- [63] Y. Horikawa and H. Kitajima, *Chaos* **22**, 033115 (2012).
- [64] T. Tamás, *Chaos* **25**, 097619 (2015).
- [65] L. A. Safonova and Y. Yamamoto, 1/f dynamics, adaptable attractor selection and synchronizability in noise-driven multistable neuronal networks, in *Proceedings of the SPIE*, Adelaide, 2006, edited by A. Bender (SPIE, Washington, 2007), p. 64170G.
- [66] Z. G. Zhao, L. L., and H. G. Gu, *Commun. Nonlinear Sci. Numer. Simulat.* **85**, 105250 (2020).
- [67] E. M. Izhikevich, *Int. J. Bifurc. Chaos* **10**, 1171 (2000).
- [68] A. Tonnelier, *Phys. Rev. E* **90**, 022701 (2014).
- [69] N. Berglund and D. Landon, *Nonlinearity* **25**, 2303 (2012).